1 **Comparison of soil characteristics from geophysical and geochemical**

2 **techniques along a climate and ecological gradient, Chilean Coastal**

3 **Cordillera (26° to 38° S)**

5 Mirjam Schaller[1][*]

6 Igor Dal Bo[2][*]

7 Todd A. Ehlers[1]

8 Anja Klotzsche[2]

9 Reinhard Drews[1]

10 Juan Pablo Fuentes Espoz[3]

11 Jan van der Kruk[2]

13 [1] Department of Geosciences, University of Tübingen, Germany,

14 Schnarrenbergstrasse 94-96, 72076 Tübingen, Germany

15 [2] Agrosphere (IBG-3), Institute of Bio- and Geosciences, Forschungszentrum

16 Jülich, 52428, Jülich, Germany

17 [3] University of Chile, Department of Silviculture and Nature Conservation, Av.

18 Santa Rosa 11315, La Pintana, Santiago RM, Chile

19 * Authors contributed equally.

21 Corresponding author: E-mail: Mirjam Schaller (mirjam.schaller@uni-

22 tuebingen.de)

25   ***Abstract***

26   In this study, we combine geophysical observations from Ground Penetrating

27   Radar (GPR) with soil physical, and geochemical properties from pedons excavated

28   in four study areas spanning 1,300 km of the climate and ecological gradient in the

29   Chilean Coastal Cordillera. Our aims are to: (1) relate GPR observations to depth

30   varying soil physical and weathering-related chemical properties in adjacent

31   pedons, and (2) evaluate the lateral extent to which these properties can be

32   extrapolated along a hillslope using GPR observations. Physical observations

33   considered include soil bulk density and grain size distribution whereas chemical

34   observations are based on major and trace element analysis. Results indicate that

35   visually-determined soil thickness and the transition from the soil B to C horizons

36   generally correlate with maximums in the 500 and 1000 MHz GPR envelope profiles.

37   To a lesser degree, these maximums in the GPR envelope profiles agree with

38   maximums in weathering related indices such as the Chemical Index of Alteration

39   (CIA) and the chemical index of mass transfer (τ) for Na. Finally, we find that up-

40   scaling from the pedon to hillslope scale is possible with geophysical methods for

41   certain pedon properties available. Taken together, these findings suggest that the

42   GPR profiles along hillslopes can be used to infer lateral thickness variations in soil

43   horizons, and to some degree the physical and chemical variations with depth.

45   Keywords: soil, saprolite, hillslope, climate, vegetation, geophysics,

46

1 Introduction

47

48   Weathering of bedrock by biotic and abiotic processes produces regolith which

49 provides resources for life. Most biota is found in an upper mobile layer (soil), which

50 is underlain by an immobile layer of weathered material (saprolite) that replenishes

51 the soil with nutrients through chemical weathering and erosion that drives nutrient

52 uplift towards the surface (e.g., Porder et al., 2007). The thickness and production

53 of soil is influenced by topography, tectonically driven rock uplift, climate, biota,

54 composition (mineral content), and time (e.g., Hilgard, 1914; Jenny, 1994).

55 However, sub-surface variations in soil thickness at the scale of hillslopes are

56 difficult to quantify because of lack of exposure. Thus, subsurface imaging by

57 geophysical techniques, when calibrated to soil pit excavations (pedons), offers one

58 potential mean to characterize spatial variability in soil thickness and soil properties

59 (e.g., Mellett, 1995; Doolittle and Collins, 1995; Miller et al., 2004). Here, we

60 evaluate the utility of applying Ground Penetrating Radar (GPR) to map variations

61 in soil properties in diverse climate and ecological settings with stark differences in

62 physical and chemical soil properties.

63   Previous work has attributed spatial variations in soil thickness to hillslope

64 curvature (Heimsath et al., 1997; Heimsath et al., 1999), which determines the

65 downslope rate of mass transport assuming a diffusion based geomorphic transport

66 law (e.g., Roering et al., 2001). However, this single point information is spatially

67 restricted and pedon excavations are time-intensive. To further understand spatial

68 variations in soil and saprolite thickness, other approaches such as modeling (e.g.,

69 Scarpone et al., 2016) and geophysical imagining (e.g., see summary in Parsekian

70 et al., 2015) have been applied. For example, soil thickness variations were

71 extrapolated from Digital Elevation Models (DEMs) in combination with several

72 different observations at single locations (e.g., Scarpone et al., 2016). Different

73 geophysical techniques have provided a non-or minimally invasive approach to view

74 soil variations down to the saprolite and bedrock interface (e.g., Parsekian et al.,

75 2015). Whereas high frequency GPR has proven suitable for investigating soil

76 layering and thickness (e.g., Doolittle et al., 2007; Gerber et al., 2010; Roering et

77   al., 2010; Dal Bo et al., 2019), other methods such as seismics (e.g., Holbrook et

78   al., 2014), Electrical Resistivity Tomography (ERT, e.g., Braun et al., 2009), and low

79   frequency GPR (e.g., Aranha et al., 2002) are better suited to image saprolite and

80   bedrock interfaces (e.g., Parsekian et al., 2015). GPR methods were previously also

81   used to indirectly measure the distribution of water flow (e.g., Zhang et al., 2014;

82   Guo et al., 2020) as well as root density (e.g., Hruska et al., 1999; Guo et al., 2013).

83   Interpreting the interplay of GPR signals with physical and chemical soil properties

84   within the sub-surface is challenging and not well-understood (e.g., Saarenketo,

85   1999; Sucre et al., 2011; Tosti et al., 2013; Sarkar et al., 2019).

86   The Chilean Coastal Cordillera (Fig. 1) contains an extreme climate and

87   vegetation gradient and it is a natural laboratory to study the influence of climate

88   and vegetation on the sub-surface of the Earth in a setting with a similar tectonic

89   history and lithology. The region is home to four study areas of the German-Chilean

90   EarthShape priority program (www.earthshape.net), where investigations of biotic

91   interactions with critical zone processes are conducted (e.g., Bernhard et al., 2018;

92   Oeser et al., 2018). The study areas were selected due to the arid climate in the

93   northernmost location (26° S), and temperate rain forest conditions in the

94   southernmost location (38° S). These four study areas are investigated to both

95   qualitatively and quantitatively describe the differences between the four settings.

96   Our previous work in these areas has so far identified increases in soil thickness

97   from north to south and major and trace element compositional variations within

98   pedons (e.g., Bernhard et al., 2018; Oeser et al., 2018; Dal Bo et al., 2019).

99   However, a detailed comparison of geophysical, geochemical, and soil observations

100   is yet to be conducted in these areas.

101   In this study, we investigate how physical as well as chemical observations

102   measured at point locations (pedons) relate to GPR observations to gain further

103   insight into the sub-surface variations. In general, we find that GPR signals can be

104   correlated to changes in soil physical properties if these changes are of sufficient

105   magnitude and laterally coherent. If such a correlation is observed, we discuss the

106   links between the physical and chemical properties. The comparison of physical and

107   chemical properties with field observations and GPR data helps to better understand

108   the sub-surface at point locations (e.g., soil thickness) and in some cases allows for

109   up-scaling point observations to the hillslope scale along a GPR measurement

110   profile.

111

112   ***2 Study areas***

113   Four primary study areas are investigated in the climatic and vegetation gradient

114   observed in the Chilean Coastal Cordillera (Fig. 1 and 2; Table 2). From N to S, the

115   four selected areas are: a) Pan de Azúcar (~26.1° S); b) Santa Gracia (~29.8° S);

116   c) La Campana (~33.0° S); and d) Nahuelbuta (~37.8° S).

117

118   2.1 General climate, vegetation, and geologic setting

119   The Chilean Coastal Cordillera with its climate and vegetation gradient is a

120   natural laboratory to study the influence of climate and vegetation on denudation

121   (Fig. 1). From N to S (~26° to 38° S), present climate ranges from arid to humid-

122   temperate. The mean annual precipitation increases from close to zero to ~1500

123   mm yr^{-1}, and mean annual temperature decreases from ~20° C to ~5° C. The flora

124   consists of small shrubs, geophytes and annual plants (Armesto et al., 1993) in the

125   N and changes to lower-stature deciduous trees and shrubs intermix with tall

126   evergreen mixed forest in the S. Vegetation cover increases from close to zero to

127   ~100%.

128   Climate and vegetation in the primary study areas changed over time from the

129   Last Glacial Maximum (LGM) to present. Mean annual precipitation during the LGM

130   was higher than at present in all four study areas (Mutz et al., 2018). Mean annual

131   temperature during the LGM was lower than at present except in the southernmost

132   study area where mean annual temperature stayed the same (Mutz et al., 2018).

133   Hence, the climate gradient observed today is comparable to the gradient during the

134   LGM. Even though the climate was wetter and cooler during the LGM, no glaciers

135   covered any of the study areas (Rabassa and Clapperton, 1990). Due to these

136 climatic changes over time, vegetation zones during the LGM were shifted
137 northward by ~5° and vegetation cover was slightly (~5-10%) lower compared to
138 present (Werner et al., 2018). This shift of vegetation zones to the N and the
139 decrease in vegetation cover also likely influenced the fauna present, but to an
140 unknown degree.

141 To compare the effect of climate and vegetation on soil thickness and GPR
142 observations, differences in lithologies need to be minimal. However, these
143 conditions are not always fulfilled and need to be taken in to account. Whereas
144 bedrocks in Pan de Azúcar, La Campana, and Nahuelbuta are granites to
145 granodiorites, the bedrocks in Santa Gracia range from Granodiorites to Gabbros
146 (Oeser et al., 2018). Hence, the parent material in Santa Gracia is lower in the SiO_2-
147 content (50-65%) in comparison to the other three study areas (SiO_2-content >65%).
148 Chemical weathering and physical erosion may be affected by this difference, which
149 in turn influences soil formation and thickness.

150

151 2.2 Soil Characteristics

152 In each study area, depth profiles from a catena consisting of three profiles on
153 the S-facing slope (top-slope, mid-slope, and toe-slope) and one profile on the N-
154 facing slope (mid-slope) were described, sampled, and analyzed (Fig. 3; see also
155 Bernhard et al., 2018; Oeser et al., 2018; Schaller et al., 2018; Dal Bo et al., 2019).

156 Previous soil studies from pedons in each area identify O, A, B, and C horizons
157 (e.g., Bernhard et al., 2018) that overlie weathered bedrock (e.g., Oeser et al.,
158 2018). In this study, we follow the approach of Riebe and Granger (2013) and refer
159 to depth profiles as regolith profiles that are composed of a mobile soil layer that
160 includes the A and B horizons, and an immobile saprolite layer represented by the
161 C horizon.

162 In Pan de Azúcar, the soil is part of a regosol and consists of a 20 to 25 cm thick
163 A and B horizon. The total organic carbon content is <0.1% (Bernhard la., 2018).
164 The observed angular fragments in the soil increase in size (> 1 mm) with depth.
165 The underlying saprolite is coarse-grained and jointed (Oeser et al., 2018). The

166   average bulk density of the soil layer is 1.3 g cm^{-3}. The cambisol in Santa Gracia

167   consists of 30 to 55 cm thick layers of soil with A and B horizons overlying the

168   saprolite (Bernhard et al., 2018). The total organic carbon content is 0.4%. Whereas

169   the A horizon consists of a silt- to fine sand-sized matrix supporting up to 2 mm

170   sized fragments, the underlying B horizon shows a transitional increase of fragments

171   to a coarse fragment-supported fine-grained matrix (Oeser et al., 2018). The

172   average bulk density is 1.5 g cm^{-3}. The soils and saprolites in La Campana form a

173   cambisol. The soil layers consisting of A and B horizons are 35 to 60 cm thick and

174   have a total organic carbon content of 1.9% (Bernhard la., 2018). The fine sand-

175   to silt-sized A horizon contains fragments of up to 3 mm. The matrix in the underlying

176   B horizon is coarsening downwards and the number of fragments increases such

177   that the horizon shifts from matrix- to clast-supported. The average bulk density is

178   1.3 g cm^{-3}. The umbrisol in Nahuelbuta consists of a 60 to 90 cm thick soil layer (A

179   and B horizons) and a readily disaggregating saprolite. The total organic carbon

180   content in these soils is 6.1% (Bernhard la., 2018). The A horizon is composed of

181   silt-sized particles forming nodular soil aggregates. In the upper part there are up to

182   1 mm large quartz grains embedded whereas the lower part contains large

183   fragments. The fine sand-sized matrix of the transitional B horizon hosts subangular

184   fragments. The amount and size of these fragments increases with depth. The

185   average bulk density of the soil layer is 0.8 g cm^{-3}.

186

187   *3 Data compilation and methods*

188   New data from 32 GPR profiles in the four study areas were collected at

189   frequencies of 500 and 1000 MHz. These data are compared to physical and

190   chemical properties from point locations (pedons) from previous studies (Bernhard

191   et al., 2018; Oeser et al., 2018). These new GPR profiles complement previous GPR

192   data collected at the same frequencies, in the same catchments (Dal Bo et al.,

193   2019). The difference between this study and that of Dal Bo et al. (2019) lies in the

194   new, more extensive, GPR data coverage and the comparison of it to physical and

195   chemical subsurface variations.

196   Using chemical and physical properties collected in pedons to understand the

197   corresponding radar signatures is a difficult task requiring treatment on multiple

198   layers. First, it would need fixed relationships translating the measured pedon

199   properties to corresponding permittivity changes relevant for the radar signal.

200   Second, it would need a radar forward model that successfully predicts the

201   convolution of the emitted radar pulse with the sub-surface reflectivity. This includes

202   among others handling constructive and destructive interference caused by closely-

203   spaced permittivity changes in the vertical. For applications on soil, this is currently

204   not possible because already the permittivity relationships are unclear. We

205   therefore take a step back from the more sophisticated methods, and use simpler

206   statistical metrics trying to isolate some properties (i.e. Pearson correlation) or

207   combinations thereof (i.e. Principal Component Analysis) that may explain parts of

208   the radar signatures.

209

210   3.1 Data compilation

211   In this study, GPR data are compared to previously published soil and saprolite

212   physical and chemical properties (Table 1) such as: 1) soil bulk density, grain size

213   distribution, pH, and cation exchange capacity - CEC (Bernhard et al., 2018); and

214   2) Loss On Ignition - LOI, Chemical index of Alteration - CIA, mass transfer

215   coefficient τ, and volumetric strain, ε_{strain} (Oeser et al., 2018). The grain size

216   distributions provide a measure of the weight percent of different grain sizes smaller

217   than 2 mm in the regolith, and the regolith bulk density provides a measure of how

218   dense the soil and saprolite material is packed. The geochemical data used provide

219   major and trace element analysis, the acid and base properties (pH) and cation

220   exchange capacity (CEC). Major and trace element analysis allow the investigation

221   of the loss on ignition (LOI), the chemical index of the mass transfer coefficient (τ),

222   and the volumetric strain (ε_{strain}). LOI is a measure of the loss of volatile substances

223   in a material due to excess heating (1000°C), thereby reflecting the amount of soil

224 organic matter. The degree of weathering can be quantified by the CIA which is
225 sensitive to the removal of alkalis such as calcium, sodium, and potassium from
226 feldspars (Nesbiitt and Young, 1982). The mass transfer coefficient (τ_{strain}) reflects
227 chemical gains and losses during weathering based on the elemental
228 concentrations of mobile and immobile elements in weathered and unweathered
229 material (e.g., Brimhall et al., 1985; Chadwick et al., 1990), ε in a regolith is based
230 on the density ρ (g cm^{-3}) and immobile element concentrations of the weathered
231 regolith in comparison to the unweathered bedrock indicating volumetric gain or loss
232 (Brimhall and Dietrich, 1987).

233

234 3.2 Ground Penetrating Radar (GPR)

235   Ground Penetrating Radar (GPR) is a geophysical technique based on the
236 emission of pulsed electromagnetic waves into the subsurface and here frequencies
237 of 500 and 1000 MHz are applied. The electromagnetic waves are reflected and
238 scattered in the presence of dielectric contrasts at depth. The back-propagated
239 reflected wave is then received at travel times, which depend on the depth-variable
240 electromagnetic wave velocity v. The velocity of the media is dictated by the relative
241 dielectric permittivity ε_r (Jol, 2009). The attenuation of the waves can be linked to
242 the electrical conductivity σ. The vertical resolution depends on the system's
243 bandwidth and the wave velocity and is in our case approximately 0.07 m for 500
244 MHz and 0.03 m for 1000 MHz. Surface GPR can be measured in two ways
245 including: 1) Common-Offset Profiling (COP) and 2) Common-midpoint (CMP) or
246 wide-angle-reflection-refractions (WARR) measurements (see also Dal Bo et al.,
247 2019). COPs measure traveltime versus spatial position along specific transects
248 with two antennae at fixed offsets. Here, this was done along profiles crossing the
249 pedons (e.g., Fig. 2 and 3). WARRs are used to retrieve velocity and physical
250 properties at the point scale with variable antennae spacing. Specifically, for each
251 pedon a WARR was measured in a relatively flat location by keeping the transmitter
252 position fixed at the pedon location and by moving the receiver towards the
253 transmitter with a step size varying between 0.01 and 0.05 m depending on the

254 deployed frequency. In such way, the move-outs of linear events (air wave and
255 ground wave) and of hyperbolic events (sub-surface reflections) could be identified
256 using the underlying assumption that internal reflectors are not dipping.

257   Twenty-eight COP transects going from hillslope toe (near valley) to top (ridge
258 crest) were collected in the four study areas using 500 and 1000 MHz GPR
259 antennae (Sensor and Software Inc.). The average trace spacing of these vary
260 between 0.01 and 0.05 m depending on frequency and location. These transects
261 were chosen in such a way as to run between pedons, where the previously
262 described physical and chemical properties were collected (Bernhard et al., 2018;
263 Oeser et al., 2018). Of these 28 profiles, two were collected in the Pan de Azúcar
264 study area, six in Santa Gracia, three in La Campana, and three in Nahuelbuta.
265 Each profile was measured twice to total 28 (at the two frequencies). The pedon
266 locations formed the basis for comparison to the GPR data as ground-truth data and
267 WARRs and COPs where collected specifically at these positions (red stars, Fig. 2).
268 Additionally, four perpendicular GPR crosslines (perpendicular to the transects)
269 were measured at both the 500 and 1000 MHz in the La Campana and Nahuelbuta
270 study areas. The position of each profile was determined using a differential GPS
271 (Leica Geosystems AG) with a maximum horizontal and vertical precisions of 2 and
272 4 cm, respectively.

273   GPR data were processed and analyzed similar to Dal Bo et al. (2019) using
274 MATLAB. The GPR data processing procedure included: frequency band-pass filter,
275 amplitude gain, background removal, and time-to-depth conversion (e.g., Jol, 2009).
276 The direct air wave between receiver and transmitter was muted. Similar to Dal Bo
277 et al. (2019), the newly measured WARR profiles at the pedon locations were
278 processed and analyzed using a combined linear move-out – hyperbolic move-out
279 approach. Ground wave and reflection velocities were picked, from which an
280 average value of GPR velocity per each study area was derived and used for the
281 time-to-depth conversion of the COP profiles (see Dal Bo et al., 2019). The
282 averaged value of GPR velocities is used to study soil depths on hillslope scale.
283 However, the use of an average will result in an over-/under-estimate of soil depths

284   on the hillslope scale. Signal envelopes were calculated using a Hilbert transform

285   (Green, 2004; Liu and Marfurt, 2007). At each pedon location, a certain number of

286   traces depending on the measurement step size (i.e. between 10 and 50) were

287   sampled for 0.5 m uphill and 0.5 m downhill the pedon and laterally averaged for

288   comparison to the pedon physical and chemical properties. The averaging assumes

289   that both chemical and GPR signatures do not change with depth across that

290   interval, an assumption that may not hold everywhere. As the GPR envelope is

291   directly related to the electric impedance (Telford et al., 1990; Jol, 2009), the

292   envelope onset and energy intervals could be compared to variations in physical,

293   and potentially chemical, soil properties.

294

295   3.3 Statistical Correlation and Principal Component Analysis

296   Comparison between the chemical and physical pedon information (Bernhard et

297   al., 2018; Oeser et al., 2018) and GPR data was conducted two different ways. First,

298   we carried out a correlation analysis using the Pearson' correlation coefficient (r).

299   More specifically, we used the bulk density, clay content, LOI, CIA, Tau (τ),

300   volumetric strain (ε_{strain}), pH, and CEC for comparison to the GPR 500 and 1000

301   MHz antennae envelope data. The GPR envelopes were resampled and averaged,

302   such that the depth intervals were the same as for the derivates of the soil data (see

303   Table S2). Furthermore, because the envelope of GPR data is sensitive to changes

304   along the vertical direction, we also calculated the vertical gradient of the ground

305   truth information at each sampled depth using a centered difference approximation.

306   Following this, the R package function corrplot (Wei, 2012) was used to calculate

307   the Pearson's correlation coefficient to identify correlations between the variables

308   (Sedgwick, 2012). This analysis was done considering the entire climate and

309   vegetation gradient and within each location. Both the original data and the

310   derivatives were used to explore which of the two approaches delivered meaningful

311   insights.

312   Second, we conducted a multivariate analysis of the data using a principal

313   component analysis (PCA; Wold et al., 1987). This was done for both the entire

314   climate gradient and within each study area using the factoextra R package
315   (Kassambara, 2017). After each PCA analysis, a scree plot was evaluated to
316   investigate how much variance was included in each principal component (PC, Bro
317   and Smilde, 2014). In this study, at least 70% of the variance was among the first
318   two PCs, which were then further analyzed. The contribution of each variable to the
319   first and second PC was computed using the eigenvalues and eigenvectors from
320   the covariance matrix (Abdi and Williams, 2010). This resulted in a plot where the
321   x-axis is PC1 and the y-axis is PC2 and each variable is displayed as a vector with
322   a specific direction and length that indicate the magnitude and direction of the
323   contribution to each PC.
324

325   ***4 Results***

326   Physical and chemical properties from pedons are shown with the 500 and 1000
327   MHz GPR profiles and their envelopes with depth as well as investigated
328   correlations and PCAs for the four study areas (Fig. 4 to 11 and supplement Figs
329   S1 to S12; and supplement Tables S1A to D, S2A to D, S3, and S4A to E). For
330   brevity, only the comparisons between pedon observations and GPR data are
331   presented for the S-facing mid-slope positions in the main text (Fig. 4, 6, 8, and 10)
332   and the remaining locations are provided in the supplementary material. Note that
333   the envelopes are averaged over the COP data, collected over a lateral distance of
334   1 m in total, and are therefore not point information. Given that the soil thickness
335   increases towards the southern study areas, the 1000 MHz GPR antennae is
336   interpreted for the (northern two) Pan de Azúcar and Santa Gracia study areas,
337   whereas in La Campana and Nahuelbuta the 500 MHz GPR signal was used
338   because it has a deeper penetration depth. However, we show results below for
339   both frequency antennas to demonstrate the difference in penetration depth and
340   resolution between the two antennae. Details for each study area (from N to S)
341   follow.
342

4.1 Pan de Azúcar (northern most study area)

In Pan de Azúcar (Fig.1, 2A), a gradual transition from the B to the C horizon was visually observed in the pedons at 20 to 40 cm whereas the mobile/immobile boundary is considered to be at 20 to 25 cm (shaded gray areas and black line, Fig. 4, Fig. S1 to S3). The available physical properties for this location do not indicate a strong change in material properties with depth. LOI and CIA indicate a minor change in properties at ~20 cm depth. A maximum in the energy envelope in the 1000 MHz frequency is present at about 20 to 30 cm that could be related to the transition of material properties between the B and C horizons and the location of mobile/immobile boundary observed in the field.

Due to the sparse depth information for bulk density and clay content, the statistical analyses for this location was not very insightful. Whereas clay content shows a medium correlation (0.54) with the 1000 MHz GPR envelope, no strong correlation between LOI, CIA, τ, and the 1000 MHz GPR envelope could be found (Table S3). In the PCA, three primary components (PC) explain over 80% of the variance (Table S4A). PC1 has the bigger contribution from CIA, clay content, and the 500 MHz envelope whereas PC2 has the bigger contribution from LOI, the 1000MHz envelope, and τ of Na and Zr (Fig. 5).

4.2 Santa Gracia

In Santa Gracia (Fig. 1, 2B), a gradual transition from the B to the C horizon was observed in the field between 20 to 60 cm depth (shaded gray region Fig. 6, Fig. S4 to S6). The boundaries between the mobile/immobile layers in the pedon were observed between 30 to 55 cm depth. Bulk density and volumetric strain show slight changes around 15 and 30 cm depth. Whereas LOI and CIA do not show any changes with depth, τ shows changes between 30 and 50 cm depth. The 500 and 1000 MHz GPR profiles and envelopes show increased irregular and strong reflections at ~25 cm (1000 MHz) and 45 cm (500 MHz) depth, and also maximums in the envelope at ~25 cm (1000 MHz) and 45 cm (500 MHz) depths. These

372 variations in the reflections and maximums in the envelopes coincide with either the
373 top or central position of the transition from the B to the C horizon.
374   A weak to moderate correlation (~0.3) between clay content as well as CIA and
375 the 1000 MHz GPR envelope is present (Table S3). Results from a PCA analysis of
376 the Santa Gracia data indicate that 3 components explain over 80% of the observed
377 variance (Table S4B). PC1 explains over 35% of the variance, and includes bulk
378 density, CIA, and the 500 and 1000 MHz envelopes (Fig. 7). PC2, explaining 31%
379 of the variance, includes clay content, LOI, and τ of Na and Zr.
380
381 4.3 La Campana
382   Field observations from the La Campana area (Fig. 1, 2C) document a layer of
383 cobbles (5 to 10 cm diameter) between the A and B horizon at a depth of ~30 cm
384 (Bernhard et al., 2018). The transition between the B to C horizons does not contain
385 rock fragments. The transition from the B to C horizon (shaded gray area, Fig. 8)
386 and the mobile/immobile boundary (black line, Fig. 8) are observed at 34 to 110 cm
387 and 35 to 60 cm, respectively (see also Fig. S7 to S9). The mobile soil layer extends
388 deeper in La Campana than in Pan de Azúcar or Santa Gracia and physical
389 properties were available for greater depths. Bulk density and grain size change
390 gradually with depth and no soil thickness could be determined. Also, LOI, CIA, and
391 τ do not show an abrupt change in regolith properties. Reflection hyperbolas and
392 irregular reflection horizons appear in the 500 and 1000 MHz GPR data at about 40
393 to 60 cm depth above the B to C horizon transition. The second peaks of the 500
394 and 1000 MHz GPR envelopes coincide with the B to C horizon transition.
395   In contrast to the previous study areas, the 500 MHz GPR envelope correlates
396 moderately with CIA (0.56), pH (-0.57), and CEC (-0.39, Table S3). Three
397 components from the PCA analysis explain about 80% of the total variance (Table
398 S4C). PC1 (~35% of the total variance) includes LOI, τ, and CEC, whereas PC2
399 (31%) contains CIA, volumetric strain, and the envelopes (Fig. 9). PC3 is dominated
400 by pH as well as τ of Zr. In general, whereas the first energy interval (1000 MHz)

401 could be attributed to the stone layer between the A and B horizon, the second

402 energy interval occurs close to (<10 cm) with the mobile/immobile boundary (Fig.

403 8).

404

405 4.4 Nahuelbuta (southernmost study area)

406   In Nahuelbuta, the B horizon contains pebbles and cobbles at around 60 to 80

407 cm depth (Bernhard et al., 2018). The B to C horizon transition appears at 50 to 100

408 cm depth (shaded gray region, Fig. 10; see also Fig. S10 to S12). The

409 mobile/immobile boundary was identified at 60 to 90 cm depth. Density

410 measurements in the pedon indicate a transition in bulk density between about 30

411 to 60 cm depth where also the grain size distribution changes. The LOI and τ

412 generally show large changes with depth, in contrast to the CIA and volumetric strain

413 which are more homogenous with depth. The 500 MHz GPR profile indicate the

414 existence of point targets/objects appearing as reflection hyperbola or undulating

415 features at depths greater than 60cm. This depth is approximately the same depth

416 at which the mobile/immobile boundary was identified, as well as changes in the

417 physical (e.g. bulk density, percent sand) and chemical (LOI, τ) properties. The

418 hyperbolas do not add up coherently during the lateral averaging and therefore do

419 not produce a significant energy interval in the average envelope. The envelope is

420 dominated by the energy intervals given by two reflections at about 30 to 50 cm

421 depth. The lower set of these energy intervals could be linked with the upper

422 physical soil boundary.

423   Results from the correlation analysis indicate the 500 MHZ GPR envelope is

424 strongly positively correlated with bulk density (0.74), strongly inversely correlated

425 with LOI (-0.6), and moderately inversely or positively correlated with clay content (-

426 0.37), pH (0.46), and CEC (-0.53) (Table S3). Results from the PCA analysis show

427 that two PC components explain ~75% of the variance. PC1 (~57 %) includes bulk

428 density, clay content, LOI, and CEC, whereas PC2 (~18 %) contains τ of Zr and pH

429 (Fig. 11; Table S4D). In general, as the 500 MHz GPR envelope signal correlates

430 well with bulk density and clay content, the envelope signal reflects changes in soil

431 properties.

432

5 Discussion

434 Here we evaluate the chemical, physical, and geophysical observations from the

435 pedons. Using this information, we attempt to up-scale information from the pedons

436 to the hillslopes scale along the GPR transects. Potential soil thickness over

437 hillslopes is discussed in light of hillslope, aspect, and the climate and vegetation

438 gradient from N to S.

439

5.1 Synthesis of GPR data with physical and chemical properties from point locations

442 GPR data image changes in material properties that could be caused by

443 changes in physical (e.g., bulk density, grain size variation, water content), or

444 potentially chemical properties (e.g., pH, CEC, CIA). The interplay between these

445 different properties can have a complicated influence on the GPR signal and

446 therefore difficult to disentangle. Disentangling any relationship between GPR data

447 and physical and chemical properties is further complicated as not all properties

448 influencing GPR data are measured (e.g., water content; Jol, 2009). In addition, the

449 determination of soil thickness (i.e., the boundary between the mobile/immobile

450 layers) in the field causes its own problems as observed changes are transitional

451 over a depth interval of 5 to 10 cm and not discrete. In the following, we start by

452 discussing if GPR data can be used to image soil thickness as well as physical and

453 chemical properties at the pedon locations where *in-situ* observations were made in

454 each study area.

455 In Pan de Azúcar (Fig. 4, 5 and Fig. S1 to S3), the locations where GPR data

456 can be compared to pedons shows low variability in the observed soil thickness (~20

457 to 30 cm) at each pedon location. Whereas the 500 MHz signal shows deep (sub-

458 soil depth) interfaces, the maximum in the 1000 MHz energy interval signal agrees

459   with the soil thicknesses observed in the field (Fig. 4 and Fig. S1 to S3). However,

460   the boundary between soil and saprolite layers is here probably too shallow to be

461   detected with the 1000 MHz antennae. An even higher frequency would be

462   favourable to detect the soil/saprolite boundary. Hence the Pearson correlations and

463   PCA results from Pan de Azúcar are restricted not only because of GPR analysis

464   but also due to restricted physical properties. The chemical and physical properties

465   correlate only weakly to moderately with the 1000 MHz envelopes (Table S3). The

466   PCA results indicate that soil bulk density is not likely correlated with either the 1000

467   MHz signal or LOI. In Pan de Azúcar, LOI does not represent soil organic matter as

468   soils of the arid zones have low or no organic matter content. The volatile loss

469   measured in the LOI is more likely associated with the combustion of carbonates.

470   In general, shallow soils in the arid zone do not show much variability in soil

471   thickness nor provide insight into the influence of physical or chemical properties on

472   GPR signals.

473   In Santa Gracia (Fig. 6, 7 and Fig. S4 to S6), the field-observed soil thicknesses

474   of the different pedons are more variable than in Pan de Azúcar. Although the 500

475   MHz and 1000 MHz GPR envelopes indicate changes at depth, the physical and

476   chemical properties observed with depth show only a few distinct changes implying

477   that the soil thickness cannot easily be determined using only physical or chemical

478   properties. The PCA indicates that most of the variance in PC1 is explained by the

479   envelope signals, bulk density, and CIA whereas PC2 is dominated by clay content

480   and τ of Na and Zr. The clay content does not seem to be a dominant factor for the

481   envelope signal, but rather represents a complex interaction between physical and

482   chemical property changes that cannot be disentangled with available data. It

483   appears that the second energy interval in the 1000 MHz envelope may agree with

484   the observed soil thickness in Santa Gracia, and (in contrast to the Pan de Azúcar

485   location) the first maximum in the 500 MHz envelope does agree with the observed

486   soil thickness. These observations again underscore that for different locations with

487   variable soil type, vegetation, and physical and chemical properties local calibration

488   between pedons and GPR data are required.

489   The determination of soil thickness from GPR data in La Campana is as difficult
490   as in the previous settings (Fig. 8, 9 and Fig. S7 to S9). The field observations
491   indicate relatively large transition zones for the B to the C horizon, and some
492   physical properties vary only weakly with depth. As a result, the determination of
493   soil thickness with physical and chemical properties is difficult, despite the moderate
494   to strong correlation of 500 MHz GPR envelopes with derivatives of physical and
495   chemical properties. Whereas the variance in PC1 is explained by bulk density, LOI,
496   τ of Na and Zr, and volumetric strain, the variance in PC2 is dominated by the
497   envelopes, CIA, pH, and CEC. Chemical properties seem to have a considerable
498   influence on GPR signals in this setting. In La Campana, the first energy interval of
499   the 500 MHz envelope is interpreted to reflect the previously described stone layer
500   whereas the second energy interval seems to match the observed soil thickness.
501   Given these uncertainties in local conditions, a clear identification of soil thickness
502   from GPR data is difficult, even with local calibration to a pedon.

503   Finally, in Nahuelbuta (Fig. 10, 11 and Fig. S10 to S12), the observed soil
504   thickness in the field is the deepest of all the four study areas and reaches from 50
505   to 100 cm. The soil thickness is easily identifiable based on physical properties. The
506   derivatives of the physical properties correlate moderately with the available 500
507   MHz envelope (Table 3). Furthermore, the chemical properties correlate weakly with
508   the GPR envelops. The variance is strongly explained by PC1 containing physical
509   properties (e.g., bulk density, clay content, LOI) and less by PC2 including chemical
510   properties (e.g., pH, τ of Na and Zr). Even so changes in properties are more
511   pronounced in Nahuelbuta than in the drier locations, a clear correlation between
512   maximums in the 500 MHz energy envelope and soil thickness is not present. The
513   second energy interval of the 500 MHz envelope best agrees with the observed soil
514   thickness. However, due to local inhomogeneities caused by intense vegetation,
515   every pedon and its attributed GPR envelope look different.

516   In summary, the 500 and 1000 MHz envelopes at point locations have the
517   potential to be used to determine soil thickness. But, the clarity with which this can
518   be done is variable and requires calibration to local pedons. Even with local

519 calibration, the relationships are not always clear (e.g., Fig. 8). Physical and
520 chemical properties with depth exert a complex interplay on measured GPR signals.
521 If a certain combination of physical and chemical properties is dominant in one
522 setting, another combination may influence the measured GPR signal. Therefore,
523 what GPR frequency works best for the individual study area due to different
524 physical and chemical properties needs to be investigated with information from
525 point locations/pedons. For the arid Pan de Azúcar and semi-arid Santa Gracia we
526 suggest using the 1000 MHz frequency (or higher), whereas for the Mediterranean
527 climate setting of La Campana and temperate Nahuelbuta the 500 MHz frequency
528 proved better. Improvements in our approach to determine soil thickness from GPR
529 data might be possible by applying multifrequency GPR techniques, which are freed
530 from antenna effects by fusion of different frequency measurements (e.g., De Coster
531 and Lambot, 2018). Nevertheless, the point information of soil thickness has the
532 potential to be up-scaled to hillslopes in some settings using GPR transects after
533 local calibration is conducted.

534

535 **5.2 Up-scaling to hillslopes**

536 Here we use insights gained from comparisons between GPR and point
537 locations to extrapolate the soil thickness along the hillslope GPR profiles (Fig. 2,
538 3). The up-scaling is carried out using a combination of amplitude and envelope
539 depth-converted profiles. To do this up-scaling, we calculated the envelope along
540 each profile. Then, using the known soil depth data from all pedons in one study
541 area, this interface was estimated along the profiles by searching for the
542 corresponding signal in the envelope at every meter. Even though the information
543 of three-point locations is at the lower limit, the combination of field observations
544 with GPR transects allows estimation of the lateral variability of soil thickness over
545 hillslopes. However, given the complications mentioned in section 5.1 (e.g., which
546 frequency GPR antenna and envelope interval to use) the up-scaling and the
547 indicated soil thickness need to be treated with care.

548   In Pan de Azúcar (Fig. 12; Supplementary Fig. S14) the observed B to C horizon

549   transition at point locations is typically between ~14 to 50 cm. No clear soil thickness

550   could be determined based on GPR profiles. Nevertheless, soil thicknesses

551   identified from 1000 MHz GPR envelopes seem to be relatively homogeneous over

552   the entire S-facing transect with an average value of 25 ±3 cm (Table 2). In contrast,

553   the N-facing transect indicates a thinner soil uphill than downhill where it reaches a

554   maximum depth of ~50 cm (Fig. S14).

555   In Santa Gracia (Fig. 13; Supplementary Fig. S15 to 17), the soil thicknesses

556   from point locations/pedons in the S-facing transect increases downslope and

557   ranges between 20 to 60 cm (Table 2). The soil thickness based on the 1000 MHz

558   GPR envelope at the top-slope position (SGPED20) decreases first downhill and

559   then increases again, thereby demonstrating laterally variability along the hillslope.

560   The soil thickness in the mid-slope position (SGPED40) is variable and reaches

561   from 25 to 50 cm. At the toe-slope position (SGPED60) a mostly constant thickness

562   of 30 cm is identified. In the N-facing transect almost no variability in soil thickness

563   (~25 cm) is observed. Even so the soil thickness based on GPR envelopes cannot

564   be used to decipher the exact soil thickness, the method still offers a close

565   approximation of soil thicknesses determined by field observations and GPR

566   profiles.

567   In La Campana (Fig. 14; Supplementary Fig. S18 to 20) the soil thickness from

568   the 500 MHz GPR envelope is 35 to 70 cm. Whereas the top- and mid-slope

569   positions in the S-facing hillslope (LCPED10 and LCPED20, respectively) show

570   variable soil thickness between 50 and 70 cm, the toe-slope position (LCPED30)

571   contains soil thicknesses between 35 and 70 cm. Relatively constant soil thickness

572   of 50 to 60 cm are identified for the N-facing mid-slope position (LCPED40). Field

573   observations do not always agree with soil thicknesses based on GPR envelopes.

574   In the La Campana location, soil thicknesses based on GPR envelopes need to be

575   considered with caution, but contain valuable information such as the existence of

576   pebble layers. However, GPR profiles show hyperbolas and continuous reflections,

577   which can be interpreted along almost all the covered length. These interfaces can

578 be reliably used to infer soil thicknesses, when a previous calibration with soil
579 pedons has been done.

580   In Nahuelbuta (Fig. 15; Supplementary Fig. S21 to 23), soil thickness in the S-
581 facing top-slope position (NAPED10) increase downhill from 60 to 110 cm. At the
582 mid-slope position (NAPED20), the soil thickness is highly variable and ranges from
583 50 to 110 cm. Soil thickness at the toe-slope position (NAPED30) is 80 to 110 cm.
584 In the N-facing mid-slope position the soil thickness ranges from 60 to 110 cm. Soil
585 thicknesses based on GPR envelopes are generally thicker than soil thicknesses
586 observed in the field and do also not agree well with thicknesses based on GPR
587 profiles. The application of GPR envelopes to determine soil thicknesses needs to
588 be treated with care in this setting. On the contrary, GPR profiles display rather
589 continuous reflections that might represent interfaces within the soil, and could
590 therefore be used to extrapolate point-scale ground-truth information over the profile
591 scale.

592

5.3 Changes of soil thickness with hillslope position, aspect, and latitude

594   The soil thickness imaged with GPR envelopes over hillslope transects reflect
595 mainly physical properties, but also chemical properties (e.g., CIA, τ). This approach
596 gives the opportunity to study non-invasively possible changes in soil thickness over
597 hillslope position, aspect, and latitude (Fig. 12 to15; Fig. S14 to S24; Table 2). Here
598 we summarize any regional trends in soil thickness between the four study areas
599 and different aspect (N- vs. S-facing) hillslopes (Fig. 2).

600   Soil thickness in a catena that develop under comparable climate and on similar
601 lithologies are expected to increase downhill (e.g., Birkeland, 1999). From the top-
602 to toe-slope position along a catena the potential for physical erosion decreases
603 downslope due to decreasing physical potential whereas the potential for deposition
604 increases. In Pan de Azúcar, the soil thickness based on the GPR envelopes in the
605 S-facing hillslope are constant, whereas the N-facing hillslope indicates soil
606 thickness increasing from top- to toe-slope. The possible slight increase in soil
607 thickness from top- to toe-slope can be explained by low denudation rates due to

608 very low precipitation rates in Pan de Azúcar. In Santa Gracia, the constantly thin
609 soils at the S-facing top-slope are in contrast to the thicker and more variable soil
610 thickness in the mid-slope position. Bernhard et al., (2018) describe an increase of
611 the A to BC horizon from top- to toe-slope in the S-facing hillslope. In Santa Gracia,
612 precipitation and minor vegetation cover may cause the increase of the soil
613 thickness downslope as well as the variable soil thickness in the mid-slope position.
614 In La Campana, the soil thickness based on GPR envelopes is highly variable.
615 Bernhard et al., (2018) observed the thickest soil also in the mid-slope position,
616 describe a disturbed hillslope with recent erosion events (e.g., possibly due to a past
617 fire and temporary mobilization of sediment). Therefore, the S-facing hillslope in La
618 Campana is a disturbed system and therefore difficult to laterally extrapolate
619 horizons. Due to the differences in soil thickness information from the different
620 methods, soil thickness changes in hillslopes from Nahuelbuta are not further
621 considered.

622   In the southern hemisphere the N-facing hillslope is expected to be slightly
623 warmer (higher solar irradiation) and drier (due to higher evaporation) than the S-
624 facing hillslope (e.g., Anderson et al., 2013). These differences in available soil
625 moisture could potentially lead to different vegetation and soil thickness. In Pan de
626 Azúcar, the soil thickness of the S- and N-facing mid-slope positions cannot be
627 attributed to differences in vegetation cover because it is absent from both the N-
628 and S-facing slopes. In Santa Gracia, however, the thicker soil in the S-facing mid-
629 slope position than in N-facing position can either be attributed to higher vegetation
630 cover in the S-facing position (e.g., Riebe et al., 2017) or subtle lithological changes
631 (e.g. Oeser et al., 2018). Different vegetation on S-facing and N-facing slope
632 positions in La Campana could explain the higher variability in soil thickness in the
633 S-facing mid-slope positions (35 to 70 cm) than the N-facing hillslope (50 to 60 cm).
634 However, the aspect-related differences in La Campana may represent local
635 heterogeneities (e.g., physical erosion) rather than a hillslope aspect-related trend
636 (Bernhard et al., 2018). Finally, in Nahuelbuta, the GPR envelopes indicate highly
637 variable, but also slightly thicker soil thickness in the S-facing than the N-facing

638 hillslopes. A higher clay content in the S-facing than the N-facing hillslope is
639 attributed to a more intense soil formation in the S-facing hillslope (Bernhard et a.,
640 2018). Differences in soil thickness on S- and N-facing hillslopes are increasing from
641 N to S in latitude due to the increasing difference of solar irradiation on evaporation,
642 vegetation, and possible frost cracking (e.g., Riebe et al., 2017).

643   Not only is there a change in soil thickness due to aspect, but also due to the
644 latitude. Soil thickness increases and is more variable from N to S in latitude due to
645 different climate and biota in each study area. Increasing precipitation rates from N
646 to S allow an increase and diversity in vegetation. From N to S in latitude, soils
647 increase in thickness and are more variable in thickness due to the influence of biota
648 (e.g., trees, burrowing animals). The increase in biota not only causes variable soil
649 thickness, but also homogenizes soils by bioturbation (e.g., Schaller et al., 2018). In
650 addition, the increase in vegetation under increasing precipitation rates causes
651 stabilization of hillslopes due to increasing precipitation rates (e.g., Langbein and
652 Schumm, 1958; Starke et al., 2020). Hillslope denudation rates derived form *in situ*-
653 produced cosmogenic nuclides increase from Pan de Azúcar to La Campana and
654 slightly decrease for Nahuelbuta (Schaller et al., 2018; Oeser et al., 2018).
655 Increasing soil thickness generally diminishes soil production rates (e.g., Heimsath
656 et al., 1997) which under steady-state conditions equal hillslope denudation rates.
657

6 Conclusions

659   Soil thickness and properties are investigated in four study areas along a climate
660 and vegetation gradient. The visually observed transition from mobile soil to
661 immobile saprolite coincides with one or more changes in measured physical and
662 chemical properties in each study area. These physical and chemical properties in
663 turn, influence return-signals generated by Ground Penetrating Radar (GPR) in the
664 sub-surface, but no systematic trend is visible for which physical or chemical
665 properties correlate with GPR based observations of soil thickness. Given this, the
666 measurements and interpretation of GPR signals for systematically identifying

667 subsurface changes in physical and chemical properties is not straightforward and

668 differs for each study area. In general, the better developed the soil the better the

669 correlation of GPR signals from point locations with physical and chemical soil

670 properties. We note that what frequency GPR antenna is best suited for identifying

671 soil thickness is difficult, and calibration to local point locations (e.g. pedons) is

672 always required. However, after local calibration between GPR signals and point

673 locations is conducted, information of soil thickness from point locations can be up-

674 scaled to hillslope transects with care.

675

676 ***Acknowledgement***

677 We would like to thank CONAF and all the Park Rangers for the possibility of working

678 in the natural parks, for providing access to the sample locations, and help inside

679 the National Parks. We acknowledge support from the German Science Foundation

680 (DFG) priority research program SPP-1803 "EarthShape: Earth Surface Shaping by

681 Biota" (sub grants KR 3725/1-1 and SCHA 1690/3-1). RD was supported by a DFG

682 Emmy Noether grant (DR 822/3-1).

683

684

685
686

687 **References:**

688 Abdi, H., and Williams, L.J. Principal component analysis, Wiley interdisciplinary
689   reviews: computational statistics 2, 433-459, 2010.

690 Anderson, S.P., Anderson, S.P., and Tucker, G.E. Rock damage and regolith
691   transport by frost: An example of climate modulation of the geomorphology of
692   the critical zone, Earth Surface Processes and Landforms, DOI:
693   10.1002/esp.3330, 2013.

694 Aranha, P.R.A., Augustin, C.H.R.R., and Sobreira, F.G. The use of GPR for
695   characterizing underground weathered profiles in the sub-humid tropics, Journal
696   of Applied Geophysics, 49, 195-210, 2002.

697 Armesto, J.J., Vidiella, P.E., and Gutierrez, J.R. Plant communities of the fog-free
698   coastal desert of Chile: plant strategies in a fluctuating environment, Revista
699   Chilena de Historia Natural, 66, 271-282, 1993.

700 Bernhard, N., Moskwa, L.-M., Oeser, R., von Blanckenburg, F., Boy, H., Brucker,
701   E., Dippold, M., Ehlers, T.A., Fuentes-Espoz J.P., Godoy, R., Köster, M., Osses,
702   P., Paulino, L., Schaller, M., Scholten, T., Seguel, O., Spielvogel, S., Spohn, M.,
703   Stock, S., Stroncik, N., Uebernickel, K., Wagner, D., Kühn, P.: Pedogenic and
704   microbial interrelations to regional climate and local topography: New insights
705   from a climate gradient (arid to humid) along the Coastal Cordillera of Chile,
706   Catena, 170, 335-355, 2018.

707 Birkeland, P.W. Soils and Geomorphology, Oxford University Press, New York,
708   1999.

709 Braun, J.-J., Descloitres, M., Riotte, J., Fleury, S., Barbiero, L., Boeglin, J.-L.,
710   Violette, A., Lacarce, E., Ruiz, L., Sekhar, M., Mohan Kumar, M.S.,
711   Subramanian, S., and Dupre, B. Regolith mass balance inferred from combined
712   mineralogical, geochemical and geophysical studies: Mule Hole gneissic
713   watershed, South India, Geochimica et Cosmochimica Acta, 73, 935-961, 2009.

714 Brimhall, G.H., and Dietrich, W.E. Constitutive mass balance relations between
715   chemical composition, volume, density, porosity, and strain in metasomatic

716   hydrochemical systems: Results on weathering and pedogenesis, Geochimica
717   et Cosmochimica Acta, 51 (3), 567-587, 1987.

718 Brimhall, G.H., Alpers, C., and Cunningham, A.B. Analysis of supergene ore-forming
719   processes using mass balance principles, Econoomic Geology, 80, 1227-1254,
720   1985.

721 Bro, R., and Smilde, A.K. Principal component analysis, Analytical Methods, 6,
722   2812-2831, 2014.

723 Chadwick, O.A., Brimhall, G.H., and Hendricks, D.M. From a black to a gray box - a
724   mass balance interpretation of pedogenesis, Geomorphology, 3, 369-390,
725   1990.

726 Dal Bo, I., Klotzsche, A., Schaller, M., Ehlers, A.T., Kaufmann, M.S., Fuentes-
727   Espoz, J.P., Vereecken, H., van der Kruk, J. Geophysical imaging of regolith in
728   landscapes along a climate and vegetation gradient in the Chilean Coastal
729   Cordillera, Catena, 180, 146-159, 2019.

730 De Coster, A., and Lambot, S. Fusion of Multifrequency GPR Data Freed From
731   Antenna Effects, Journal of Selected Topics in Applied Earth Observations and
732   Remote Sensing, 11 (2),.664-674, 2018.

733 Doolittle, J.A., and Collins, M.E. Use of soil information to determine application of
734   ground penetrating radar. Journal of Applied Geuphysics, 33 (1-3), 101-105,
735   1995.

736 Doolittle, J.A., Minzenmayer, F.E., Waltman, F.W., Benham, E.C., Tuttle, J.W., and
737   Peaslee, S.D. Ground-penetrating radar soil suitability map of the conterminous
738   United States, Geoderma, 141, 416-421, 2007.

739 Gerber, R., Felix-Henningsen, P., Behrens, T., and Scholten, T. Applicability of
740   ground-penetrating rader as a tool for nondestructive soil-depth mapping on
741   Pleistocene slope deposits, Journal of Plant Nutrition and Soil Science, 173 (2),
742   173-184, 2010.

743 Green, A.G. Applications of 3-D georadar methods to diverse environmental and
744   engineering problems, Progress in Environmental and Engineering Geophysics,
745   edited by Chao, C. and Jianghai, X., Science Press USA, 220-226, 2004.

746   Guo, L., Chen, J., Cui, X., Fan, B., and Lin, H. Application of graound penetrating
747   radar for coarse root detection and quantification: a review, Plant Soil, 362, 1-
748   23, 2013.

749   Guo, L., Mount, G.J, Hudson, S., Lin, H., and Levia, D. Pairing geohpysical
750   techniques helps understanding of the near-surfce Critical Zone: Visualization
751   of preferential rouging of stemflow along coarse roots. Geoderma, 357, 113953,
752   2020.

753   Heimsath, A.M., Dietrich, W.E., Nishiizumi, K., and Finkel, R.C. The soil
754   productionfunction and landscape equilibtium, Nature, 388, 358-361, 1997.

755   Heimsath, A.M., Dietrich, W.E., Nishiizumi, K., and Finkel, R.C. Cosmogenic
756   nuclides, topography, and the spatial variation of soil depth, Geomorphology,
757   27, 151-172, 1999.

758   Hilgard, E.W. Soils: Their Formation, Properties, Compositions and Relations to
759   Climate and Plant Growth in the Humid and Arid Regions, The Macmillan
760   Company, New York, 1914.

761   Holbrook, W.S., Riebe, C.S., Elwaseif, M., Hayes, J.L., Vasler-Reeder, K., Harry,
762   D.L., Malazian, A., Dosseto, A., Hartsough, P.C., and Hopmans, W.
763   Geophysical constraints on deep weathering and water storage potential in the
764   Southern Sierra Critical Zone Observatory. Earth Surface Processes and
765   Landforms, 39, 366-380, 2014.

766   Hruska, J., Cermak, J., and Sustek, S. Mapping tree root system with ground-
767   penetrating radar. Tree Physiology, 19, 125-130, 1999.

768   Jenny, H. Factors of Soil Formation: A System of Quantitative Pedology, Dover
769   Publications, New York, 1994.

770   Jol, H.M. (Ed.): Ground penetrating radar: theory and applications, Elsevier Science,
771   Amsterdam, the Netherlands ; Oxford, United Kingdom, 2009.

772   Kassambara, A. Practical guide to cluster analysis in R: unsupervised machine
773   learning, STHDA, 2017.

774   Langbein, W.B., and Schumm, S.A. Yield of sediment in relation to mean annual
775   precipitation, Transaction American Geophysical Union, 39, 1076-1084, 1958.

776 Liu, J.L., and Marfurt, K.J. Instantaneous Spectral Attributes to Detect Channels,
777   Geophysics, 72, 23-31.
778   http://dx.doi.org/10.1190/1.2428268, 2007.

779 Mellett, J.S. Ground penetrating radar applications in engeneering, environmental
780   management, and geology, Journal of Applied Geophysics, 33 (1-3), 157-166,
781   1995.

782 Miller, T.W., Hendrickx, J.M.H., and Borchers, B. Radar detection of burried
783   landmines field soils. Vadose Zone Journal, 3 (4). 1116-1127, 2002.

784 Mutz, S.G., Ehlers, T.A., Werner, M., Lehmann, G., Stepanek, C., and Li, J. Where
785   is Late Cencozoic climate change most likely to impact denudation?, Earth
786   Surface Dynamics, 6, 271-301, https://doi.org/10.5194/esurf-2017-47, 2018.

787 Oeser, R.A., Stroncik, N., Moskwa, L.-M., Bernhard, N., Schaller, M., Canessa, R.,
788   van der B Rin, L., Köster, M., Brucker, E., Stock, SS., Fuentes, J..P., Godoy, R.,
789   Matus., F.J., Oses Pedraza, R., Osses McIntyre, P., Paulino, L., Seguel, O.,
790   Bader, M.Y., Boy, J., Dippold, M.A., Ehlers, T.a., Kühn, P., Kuzyakiv, Y.,
791   Peinweber, P., Scholten, T., Spielvogel, S., Spohn, M., Üubernickel, K.,
792   Tielbörger, K., Wagner, D., and von Blanckenburg, F. Chemistry and
793   microbiology of the Critical Zone along a steep climate and vegetation gradient
794   in the Chilean Coastal Cordillera, Ctena, 170, 183-203, 2018.

795 Parsekian, A.D., Singha, K., Minsley, B.J., Holbrook, W.S., and Slater, L. Multiscale
796   geophysical imaging of the critical zone, Reviews of Geophysics, 53, 1-26,
797   2015.

798 Porder, S., Vitousek, M.P., Chadwick, O.A., Chamberlain, C. P. and Hilley, G.E.
799   Uplift, Erosion, and Phosphorous Limitation in Terrestrial Ecosystems,
800   Ecosystems, 10, 158-170, 2007.

801 Rabassa, J., and Clapperton, C.M. Quaternary glaciations of the southern Andes,
802   Quaternary Science Reviews, 9, 153-174, 1990.

803 Riebe, C.S., and Granger, D. Quantifying deep and near-surface chemical erosion
804   on cosmogenic nuclides in soils, saprolite, and sediment, Earth Surface
805   Processes and Landforms, 38, 523-533, 2013.

806 Riebe, C.S., Hahm, W.J. and Brantley, S.L. Controls on deep critical zone
807   architecture: a historical review and four testable hypothesis, Earth Surface
808   Processes and Landforms, 42, 128-156, 2017.

809 Roering, J.J., Kirchner, J.W., and Dietrich, W.E. Hillslope evolution by nonlinear,
810   slope-dependent transport: Steady state morphology and equilibrium
811   adjustment timescales, Journal of Geophysical Research, 106, B8, 16499-
812   16513. 2001.

813 Roering, J.J., Marshall, J., Booth, A.M., Mort, M., and Jin, Q. Evidence for biotic
814   controls on topography and soil production, Earth and Planteray Science
815   Letters, 289, 183-190, 2010.

816 Saarenketo, T. Electrical properties of water in clay and silty soils. Journal of Applied
817   Geophysics, 40, 73-88, 1998.

818 Sarkar, R., Paul, K.B., and Higgins, T.R. Impacts of soil physiochemical properties
819   and temporal-seasonal soil-environmental status on ground-penetrating radar
820   response. Soil Science Society of America Journal, 83, 542-554, 2019.

821 Scarpone, C., Schmidt, M.G., Bulmer, C.E., and Knudby, A. Modelling soil thickness
822   in the critical zone for Southern British Columbia, Geoderma, 282, 59–69, 2016.

823 Schaller, M., Ehlers, T., Lang, K., Schmid, M., and Fuentes-Espoz, J. Addressing
824   the contribution of climate and vegetation cover on hillslope denudation, Chilean
825   Coastal Cordillera (26°–38° S), Earth and Planetary Science Letters, 489, 111-
826   122, 2018.

827 Sedgwick, P. Pearson's correlation coefficient, BMJ, 345:e4483, 2012.

828 Starke, J., Ehlers, T.A., and Schaller, M. Latitudinal effect of vegetation on erosion
829   rates identified along western South America. Science, 367, 1358-1361, 2020.

830 Sucre, E.B., Tuttle, J.W., and Fox, T.R. The use of ground-penetrating radar to
831   accurately estimate soil depth in rocky forest soils. Forest Science 57 (1), 59-
832   66, 2011.

833 Telford, W.M., Geldart, L.P., Sheriff, R.E. and Keys, D.A. (Eds.): Applied
834   Geophysics, 2th Edition, Cambridge University Press, Cambridge, 770.
835   http://dx.doi.org/10.1017/CBO9781139167932, 1990.

836 Tosti, F., Patriarca, C., Slob, E., Benedetto, A., and Lambot, S. Clay content
837   evaluation in soils through GPR signal processing. Journal of Applied
838   Geohpysics, 97, 69-80, 2013.
839 Wei, T. Package 'corrplot'-Visualization of a correlation matrix. v0.60. cran. rproject.
840   org, 2012.
841 Werner, C., Schmid, M., Ehelrs, T.A., Fuentes-Espoz, J.P., Steinkamp, J., Forrest,
842   M., Liakka, J., Maldonado, A., and Hickler, T. Effect of changing vegetation and
843   precipitation on denudation - Part1; Predicted vegetation composition and cover
844   over the last 21 thousand years along the Coastal Cordillera of Chile, Earth
845   Surface Dynamics, 6, 829-858, https://doi.org/10.5194/esurf-6-829-2018, 2018.
846 Wold, S., Esbensen, K., and Geladi, P. Principal component analysis,
847   Chemometrics and intelligent laboratory systems, 2, 37-52, 1987.
848 Zhang, J., Lin, H., and Doolittle, J. Soil layering and preferential flow impacts on
849   seasonal changes of GPR signals in two contrasting soils. geoderman, 213,
850   560-569, 2014.

851

852

853

854 **Figure captions**

855 Fig. 1:

856 Digital elevation model (Data source: GTOPO30) for the Chilean Coastal Cordillera

857 and the Central Andes showing the four investigated study areas (from N to S): Pan

858 de Azúcar (~26° S); Santa Gracia (~30° S); La Campana (~33° S); and Nahuelbuta

859 (~38° S).

860

861 Fig. 2:

862 Satellite images (Data source: Google Earth©) of the four study areas from N to S

863 in latitude: A) Pan de Azúcar; B) Santa Gracia; C) La Campana; and D) Nahuelbuta.

864 Red stars indicate the pedon positions whereas the blue lines represent the

865 locations of the geophysical investigations.

866

867 Fig. 3:

868 N- and S-facing hillslopes of the four study areas with locations of soil pedons and

869 transects of ground penetrating radar indicated by the red double arrows.

870

871 Fig. 4:

872 Compilation of physical and chemical investigations with depth at the pedon location

873 in the mid-slope position of the S-facing hillslope in Pan de Azúcar. Properties

874 shown are: 1) GPR transect and the envelope profile of the 500 MHz measurement;

875 2) GPR transect and the envelope profile of the 1000 MHz measurement; 3) Bulk

876 density; 4) Grain size distribution of sand, silt, and clay; 5) Loss on ignition LOI; 6)

877 Chemical index of alteration CIA 7) Chemical index of the mass transfer coefficient

878 Tau τ; and 8) volumetric strain ε_{strain}. The black line indicates the boundary between

879 the mobile soil and the immobile saprolite (after Oeser et al., 2018) and the gray

880 area with green lines reflects the transition zone from B to C horizon (after Bernhard

881 et al., 2018).

882

883 Fig. 5:

884 Primary component analysis PCA of properties for all four soil pedons in Pan de

885 Azúcar. A) Scree plot showing the percentage of explained variances and B)

886 Variables - PCA.

887

888 Fig. 6:

889 Compilation of physical and chemical investigations at the pedon location in the mid-

890 slope position of the S-facing hillslope in Santa Gracia. Properties shown are listed

891 in caption of Fig. 4.

892

893 Fig. 7:

894 Primary component analysis PCA of properties for all four soil pedons in Santa

895 Gracia.

896

897   Fig. 8:

898   Compilation of physical and chemical investigations at the pedon location in the mid-

899   slope position of the S-facing hillslope in La Campana. Properties shown are listed

900   in in caption of Fig. 4.

901

902   Fig. 9:

903   Primary component analysis PCA of properties for all four soil pedons in La

904   Campana.

905

906   Fig. 10

907   Compilation of physical and chemical investigations at the pedon location in the mid-

908   slope position of the S-facing hillslope in Nahuelbuta. Properties shown are listed

909   as in caption of Fig. 4. Note that only the 500 MHz signal and envelope profile exist.

910

911   Fig. 11:

912   Primary component analysis PCA of properties for all four soil pedons in

913   Nahuelbuta.

914

915   Fig. 12:

916   A) 1000 MHz GPR transect and B) envelope for the S-facing hillslope in Pan de

917   Azúcar. The hillslope transect spans over ~20 m and includes pedon AZPED60,

918   AZPED50, and AZPED40 (black boxes). The potential soil thickness based on the

919   envelopes is indicated by stars (in B). The red bar indicates the B to C horizon

920   transition as given in Bernhard et al. (2018). Uphill is from left to right. Note that in

921   the radar data the air wave and background removal is applied.

922

923   Fig. 13:

924   1000 MHz GPR signal and envelope for the mid-slope position of the S-facing

925   hillslope position in Santa Gracia (SGPED40). The hillslope transect spans over ~20

926   m. Interpretation of the radar signal are indicated where possible (stippled lines in A

927   and B). The potential soil thickness is indicated based on the envelope profile. Uphill

928   is from left to right. Lines and symbols in figures as described in Fig. 12.

929

930   Fig. 14:

931   500 MHz GPR signal and envelope for the mid-slope position of the S-facing

932   hillslope in La Campana (LCPED20). The hillslope transect spans over ~8 m.

933   Interpretation of the radar signal are indicated where possible (stippled and black

934   lines in A and B). The potential soil thickness is indicated based on the envelope

935   profile. Uphill is from left to right. Lines and symbols in figures as described in Fig.

936   12.

937

938   Fig. 15:

939   500 MHz GPR signal and envelope for the mid-slope position of the S-facing

940   hillslope in Nahuelbuta (NAPED20). The hillslope transect spans over ~20 m.

941   Interpretation of the radar signal are indicated where possible (stippled lines in A

942   and B). The potential soil thickness is indicated based on the envelope profile. Uphill

943   is from left to right. Lines and symbols in figures as described in Fig. 12.

944

945

946   Fig. 1:
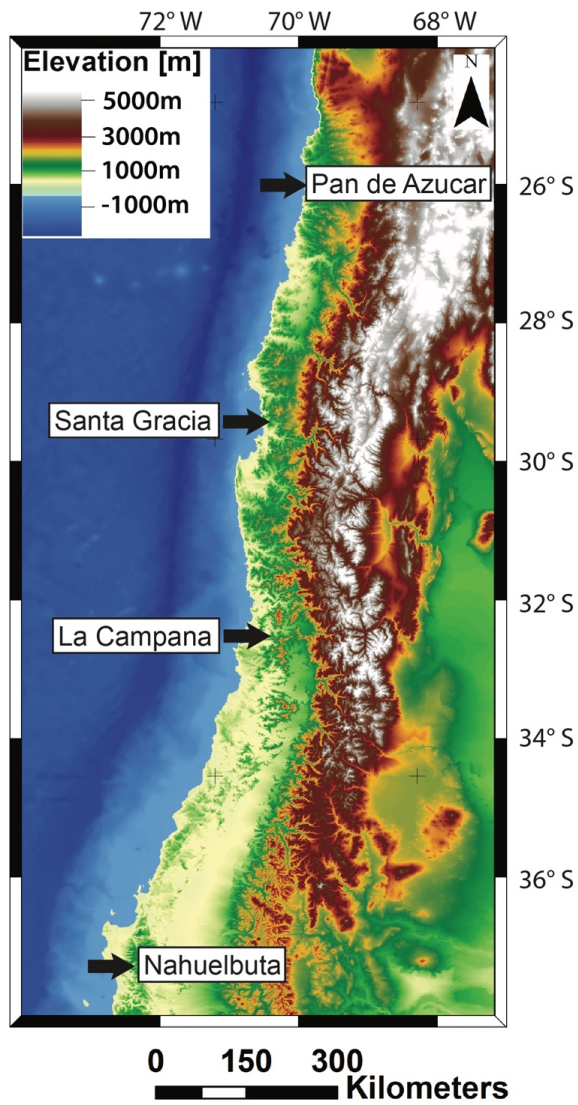
947
948

949   Fig. 2:
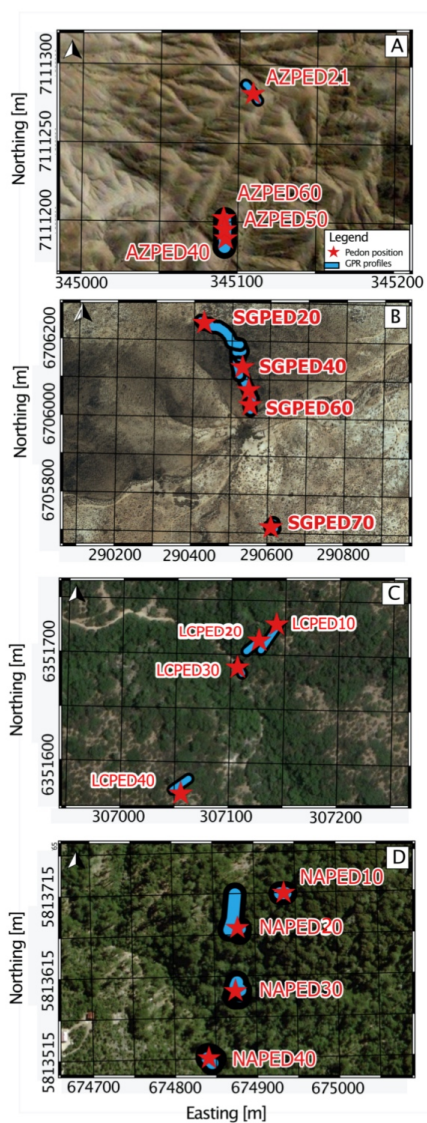
950

951   Fig. 3:
952
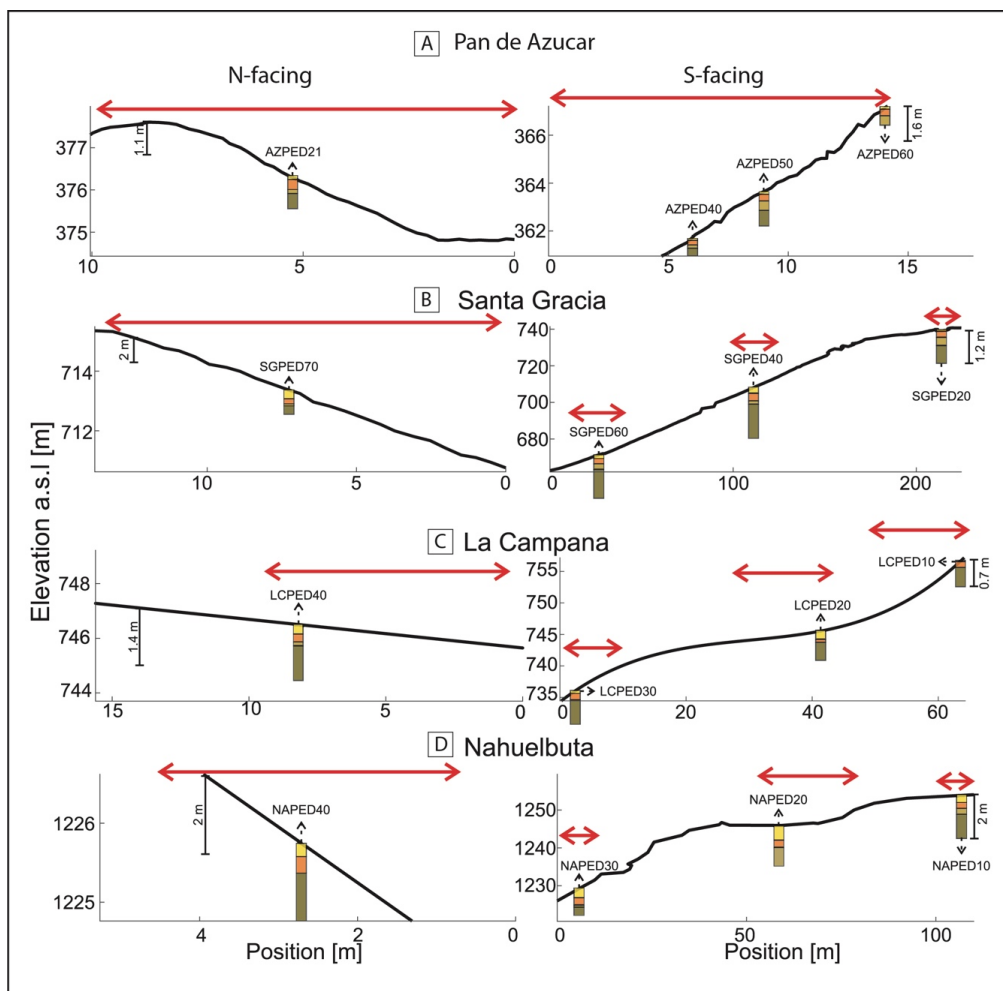
953
954

955
956
957 Fig. 4:
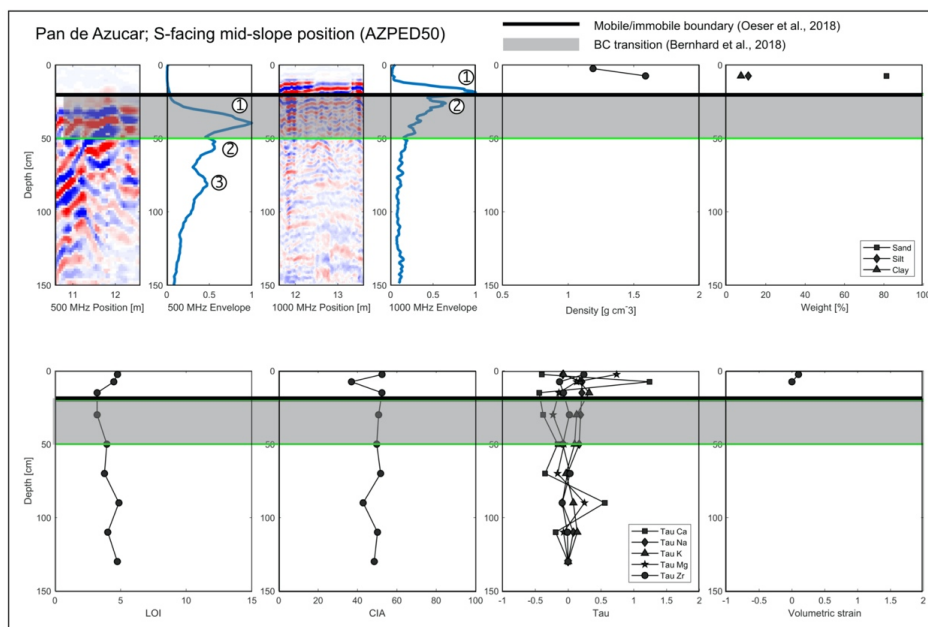
958
959
960 Fig. 5:
961
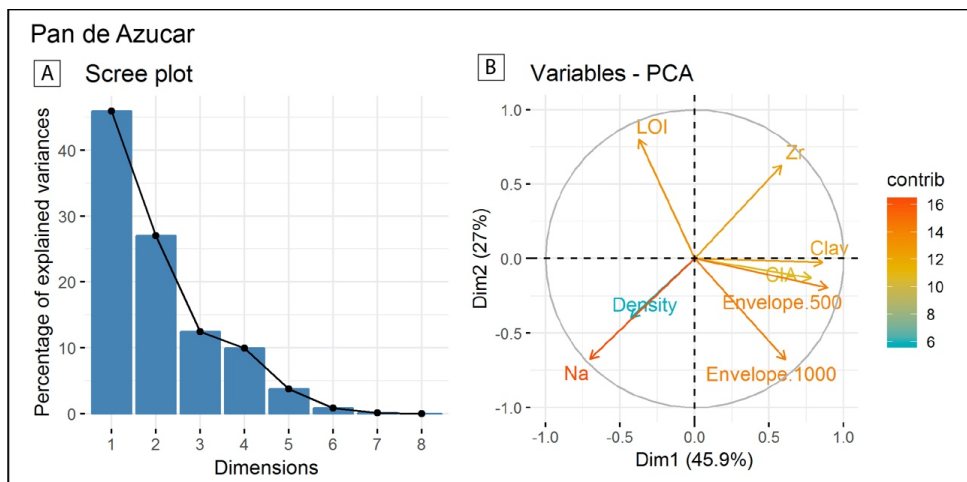
962

963
964
965
966   Fig. 6:
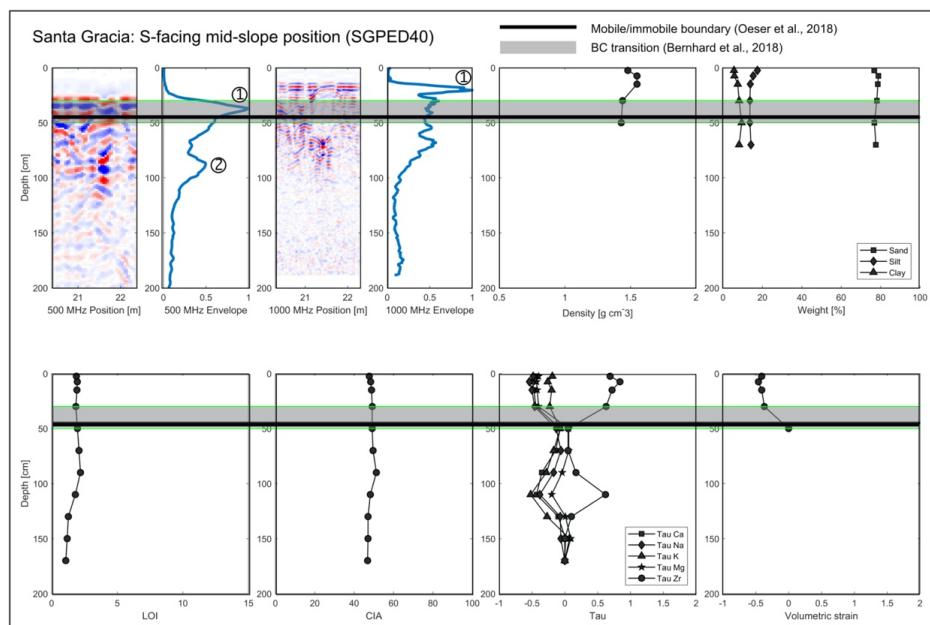
967
968
969   Fig. 7:
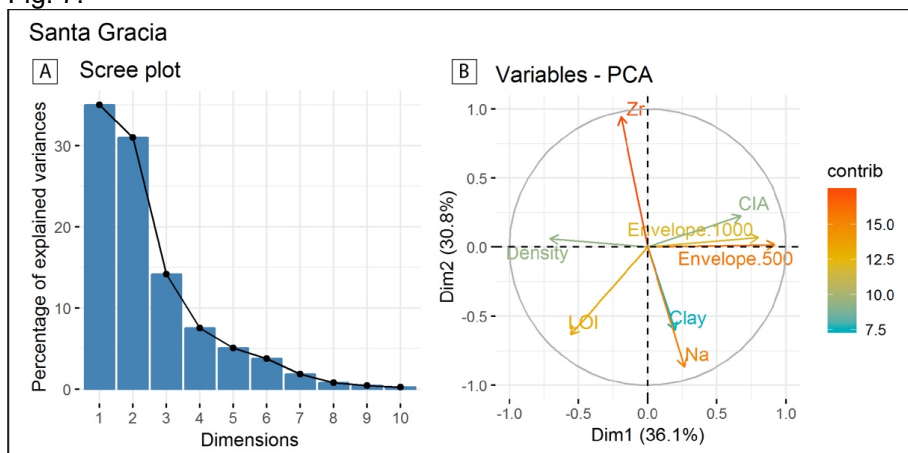
970

971
972
973
974
975
976   Fig. 8:
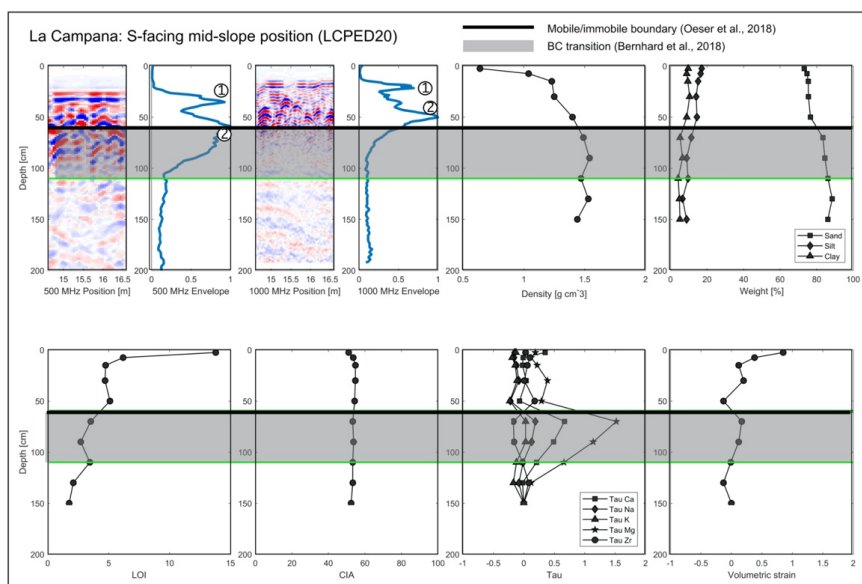
977
978
979   Fig. 9:
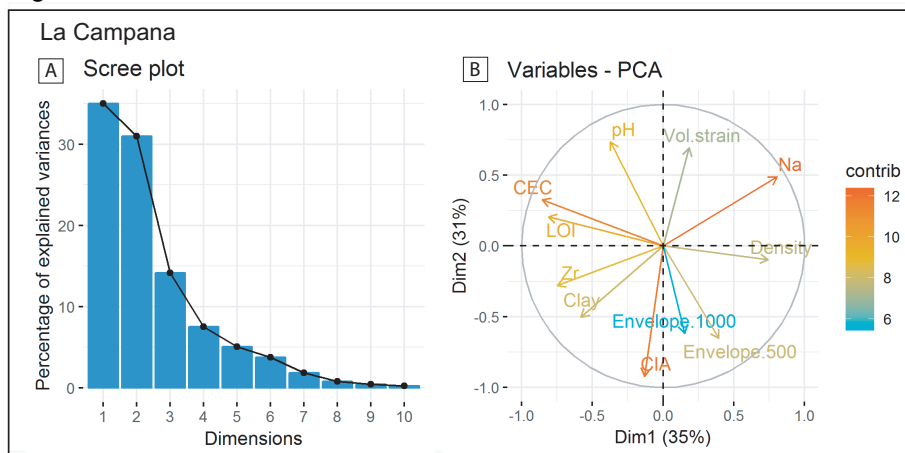
980

981   Fig. 10:
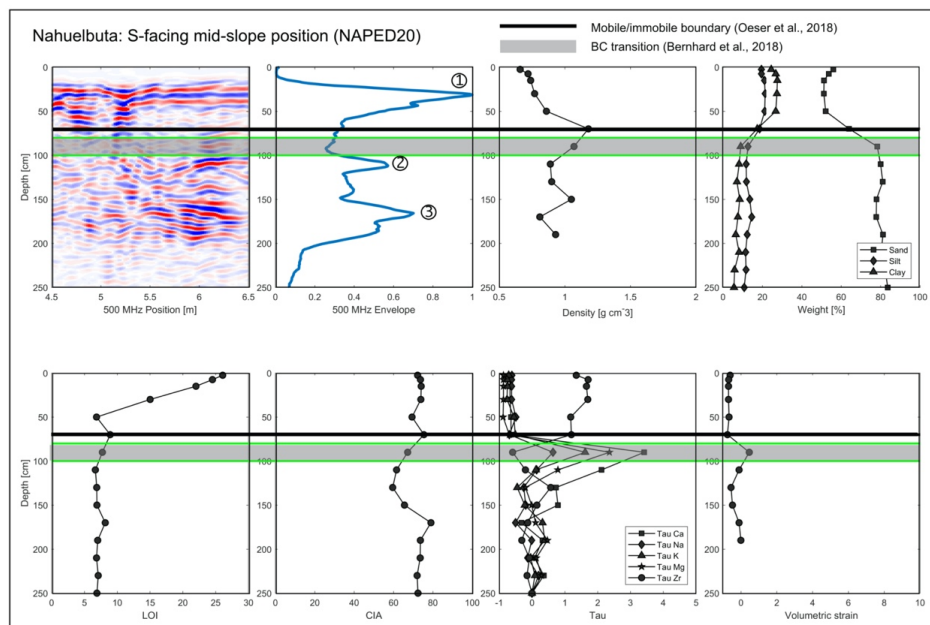
982
983
984   Fig. 11:
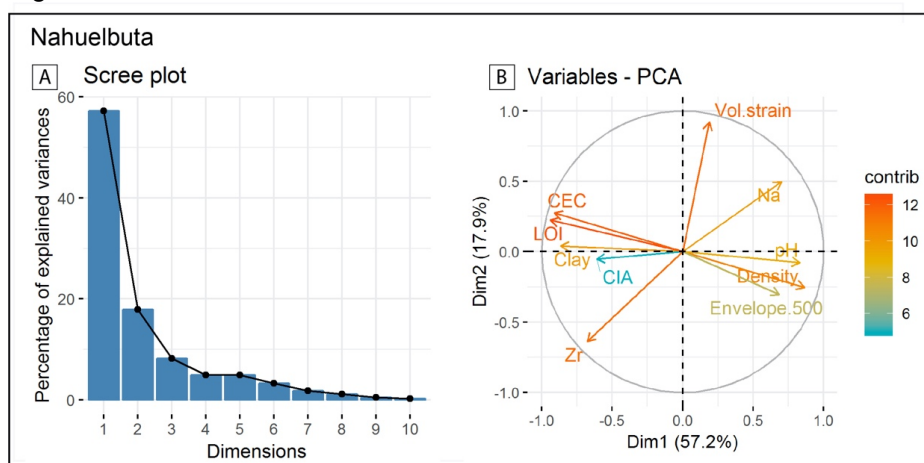
985
986
987
988

989   Fig. 12:
990
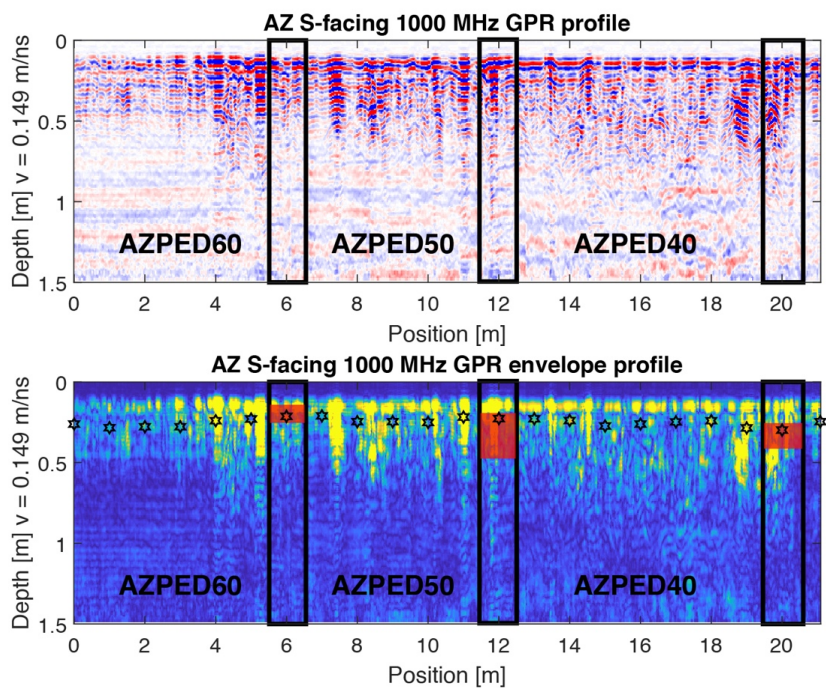
991
992
993

994   Fig. 13:
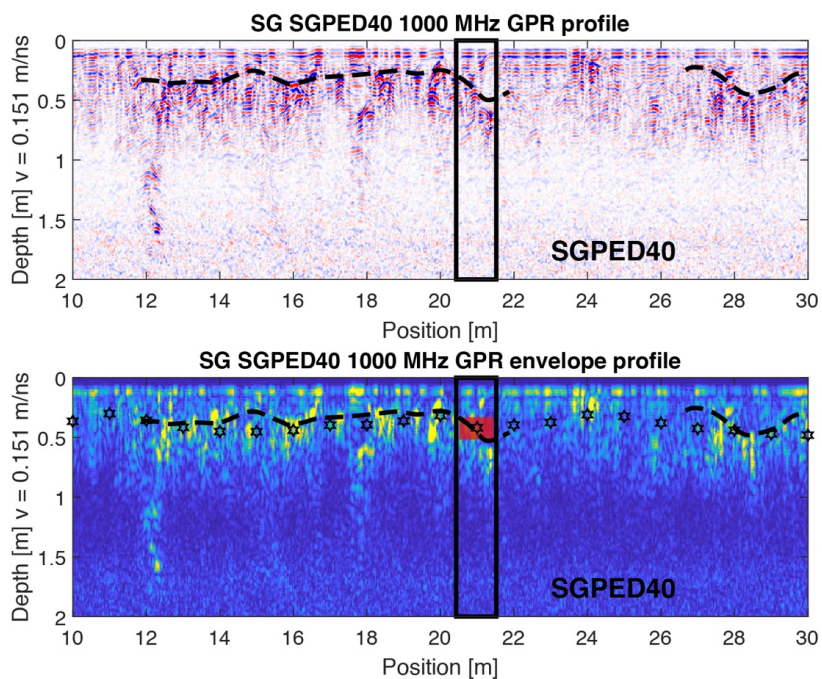
995
996

997   Fig. 14:
998
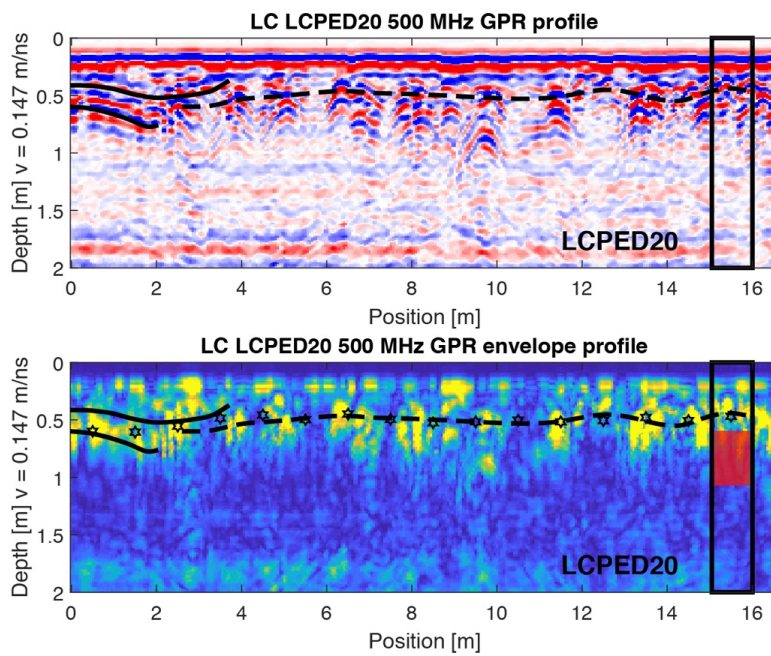
999
1000
1001

1002   Fig. 15:
1003
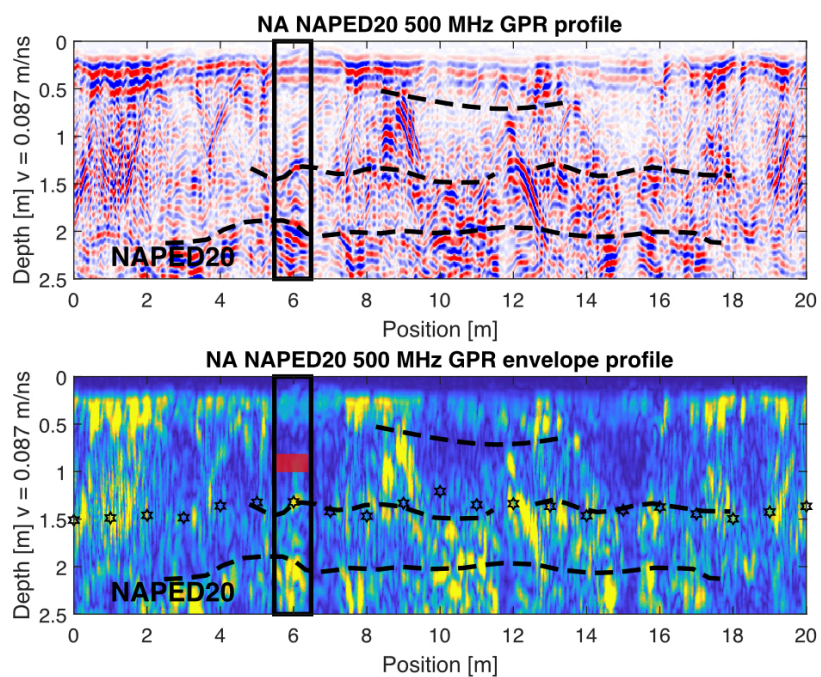
1004
1005

1006 Table 1:

1007

Table 1: Overview of physical, chemical, and geohpysical properties determined in the four different study areas				
Property	Abreviation	Units	Meaning	Reference
Soil bulk density	ρb	g/cm^3	Weight of unit volume	Bernhard et al., 2018
Grain size distributioin	GSD	%	Weight percent of different grain sizes smaller than 2 mm	Bernhard et al., 2018
Potential hydrogene	pH		Acid and base properties	Bernhard et al., 2018
Cation exchange capacity	CEC	$cmol_c/kg$	Soil ability to hold positively charged ions	Bernhard et al., 2018
Loss on ignition	LOI	%	Loss of volatiles due to excessiv heating	Oeser et al., 2018
Chemical index of alteration	CIA		Degree of weathering	Oeser et al., 2018
Mass transfer coefficient	τ	m/s	Chemical gain or loss	Oeser et al., 2018
Volumetric strain	ε_{strain}		Volumetric grain or loss	Oeser et al., 2018
Electric permitivity	ε_r		Structural changes, porosity/soil water content	Dal Bo et al., 2019; This study
Electrical conductivity	σ	mS/m	Clay, salinity	Dal Bo et al., 2019; This study

1008
1009
1010
1011
1012
1013
1014 Table 2:

Soil profile	Location		Altitude	Position	Aspect	Slope	Field observations			GPR[4]	GPR point depth[5]		GPR transect depth[6]	
							BC-horizon transition[1]	Mobile/immob.[2]	Mobile/immob.[3]		500 MHz	1000 MHz	500 MHz	1000 MHz
	°S	°W	m		°	°	cm	cm	cm	cm	cm	cm	cm	cm
Pan de Azucar														
AZPED60	26.11012	70.54922	343	top	60	5	14-26		22	30-55 (?)	40	20/25/45		
AZPED50	26.11027	70.54922	333	mid	0	40	20-50	20	20	20-55	40/50/70	20/25/35/45	36 ± 1	25 ± 3
AZPED40	26.11024	70.54921	326	toe	0	33	23-40		25	20-40	40/55	20/30		
AZPED21	26.10936	70.54907	342	mid	180	25	20-30	20	20	30-45	37/55/75	20/30/45/55	40 ± 2	28 ± 7
Santa Gracia														
SGPED20	29.75636	71.16721	718	top	240	5	20-30		30	30	40	20/30/40/50	37 ± 5	34 ± 3
SGPED40	29.75738	71.16635	682	mid	0	25	30-50	50	45	60	45	20/30/40/55/65	40 ± 7	36 ± 5
SGPED60	29.75826	71.16615	638	toe	0	20	40-60		55	-	37/50	20/30	39 ± 7	35 ± 6
SGPED70	29.76120	71.16559	690	mid	180	15	25	35	35	NA	40	20/30	35 ± 3	28 ± 2
La Campana														
LCPED10	32.95581	71.06332	734	top	60	7	34		45	40/50	35/50/70	20/30/35/50/65	55 ± 6	44 ± 5
LCPED20	32.95588	71.06355	718	mid	0	23	60-110	60	60	50/60	35/60/70	20/38/50	59 ± 6	45 ± 4
LCPED30	32.95615	71.06380	708	toe	60	35	34-55		55	45/50	35/70	20/30/38	50 ± 9	41 ± 4
LCPED40	32.95720	71.06425	724	mid	120	12	36-103	35	35	-	35/65	20/30/40	56 ± 6	47 ± 6
Nahuelbuta														
NAPED10	37.80735	73.01285	1248	top	60	5	50-75		70	70/75	35/45/120		82 ± 15	
NAPED20	37.80770	73.01357	1239	mid	60	15	80-100	95	70	75/95	35/110/170		101 ± 8	
NAPED30	37.80838	73.01345	1228	toe	0	20	63-85		90	-	5/90/120/140		96 ± 6	
NAPED40	37.80904	73.01380	1200	mid	180	13	65-90	70	60	40/50	40/80/120		95 ± 11	

Table 2: Data compilation for pedons in the investigated four study areas in the Chilean Coastal Cordillera

[1] Depth of BC-horizon transition from Bernhard et al., 2018
[2] Depth of mobile layer from Schaller et al., 2018
[1] Depth of mobile layer from Oeser et al., 2018
[4] Depth based on data from Dal Bo et al., 2019
[5] Depth based on single point GPR envelopes (This study)
[6] Average depth based on envelopes from GPR transect data (This study)

1015
1016
1017
1018

1019